ChemBioChem

Chemistry Europe
European Chemical Societies Publishing
ChemBioChem

RESEARCH ARTICLE OPEN ACCESS

Synthesis of Polyhydroxylated Pyrrolidinyl Analogs of Sugar Nucleotides. Experimental and Computational Studies on Their Interactions With GalNAC-T's

Pedro Merino[1,2] | Veronica Juste[1,2] | Alejandro Montesa[1,2] | Sandra Pereira[1,2] | Sara Orta[2,3] | Manuel Pedrón[1,2] | Ana I. Jiménez[3] | Sonsoles Martín-Santamaría[4] | Ramón Hurtado-Guerrero[1] | Ignacio Delso[3] | Tomás Tejero[2,3]

[1]Unidad de Glicobiología, Instituto de Biocomputación y Fisica de Sistemas Complejos (BIFI), Universidad de Zaragoza, Zaragoza, Spain | [2]Departamento de Química Orgánica, Facultad de Ciencias, Universidad de Zaragoza, Zaragoza, Spain | [3]Departamento de Síntesis y Estructura de Biomoléculas, Instituto de Síntesis Quimica y Catálisis Homogénea (IQCH), Universidad de Zaragoza-CSIC, Zaragoza, Spain | [4]Departamento de Biociencias Celulares y Moleculares, Centro de Investigaciones Biológicas Margarita Salas, CSIC, Madrid, Spain

Correspondence: Pedro Merino (pmerino@unizar.es)

Received: 11 December 2025 | **Revised:** 18 January 2026 | **Accepted:** 19 January 2026

Keywords: GalNAc-Ts inhibitors | molecular dynamics | nucleotide analogs | pyrrolidines | saturation transfer difference nuclear magnetic resonance

ABSTRACT

Direct coupling between polyhydroxylated pyrrolidinyl β-amino phosphonates and uridine monophosphate (UMP) yields polyhydroxylated pyrrolidinyl analogs of sugar nucleotides suitable inhibitors of *N*-acetyl-galactosyltransferases. β-Amino phosphonates have been synthesized in an enantiomerically pure form through the nucleophilic addition of a phosphonate to polyhydroxylated cyclic nitrones. The reaction has been studied in detail and excellent diastereoselectivities are obtained in agreement with a stereochemical model well supported by density functional theory calculations. Binding of the nucleotide analogs with *N*-acetylgalactosyltransferases GalNAc-T2, GalNAc-T14, and GalNAc-T16 has been studied both experimentally and computationally through molecular dynamics simulations. Saturation transfer difference nuclear magnetic resonance experiments and measurement of K_d values have been used to validate the binding model at the active site. These studies provide important information of the role of the pyrophosphate and pyrrolidinyl moieties on the observed affinity.

1 | Introduction

Mucins are glycoproteins expressed on the epithelia that provide protective barrier against toxins and pathogens [1]. Their glycoslation plays a crucial role in several biological processes [2] and they are involved in pathophysiological functions such as inflammation [3] and cancer [4]. The glycosylation of mucins is directly involved in situations as different as vision [5] and the gastrointestinal barrier against infections [6]. Mucin *O*-glycosylation is initiated by a large family of redundant UDP GalNAc:polypeptide α-*N*-acetylgalactosaminyltransferases (ppGalNAcTs) [7] classified as GT25 that target different proteins and are differentially expressed in cells and organs [8]. These enzymes are retaining glycosyl transferases dependent upon UDP-GalNAc, manganese, and proteins containing mucin-like domains [9, 10] and have been shown to be important in eukaryotic development [11], vascular biology [12], humoral immunity [13], energy homeostasis [14], lipid metabolism [15], and tumoral processes [16]. Modifications of the activity of enzymes responsible for the key glycosylation step, ppGalNAcTs, constitute a well-established molecular target against several disorders [17] including Alzheimer's disease [16], colon [18], renal [19] and laryngeal adenocarcinomas [20], gastric carcinogenesis [21], and chronic lung diseases in which an overexpression of these enzymes has been described, leading to dehydrated mucus [22].

Dedicated to the memory of Prof. Alessandro Dondoni.

Consequently, specific and potent inhibitors of ppGalNAcTs are excellent tools to explore the biological role of mucin glycosylation [23]. Among the several glycosyltransferase inhibitors reported in the last years [24], only few of them [25] have been directed against α-*N*-acetylgalactosaminyltransferases [26]. In this context, we explored analogs **1a** lacking β-phosphate as ligands of GalNAc-T2 [27] and compounds **2** as bisubstrate inhibitors (Figure 1) [28]. In a parallel approach, we also identified compounds **1b** as suitable ligands for *O*-GlcNAc transferase [29], corroborating that a protected polyhydroxylated pyrrolidine ring enhanced the affinity in the active site [30]. In this article, we report an efficient synthetic approach to sugar-UDP analogs **3** from cyclic nitrones using β-amino phosphonic acids **4** as key intermediates. The affinity between ppGalNAcTs and analogs **3** has also been studied experimentally (binding studies and saturation transfer difference nuclear magnetic resonance (STD-NMR)) and computationally (docking and molecular dynamic (MD) simulations).

2 | Results and Discussion

Few approaches have been reported for the synthesis of pyrrolidinyl β-amino phosphonic acids. Compounds unsubstituted at the pyrrolidine ring can be easily prepared from proline [31–35]. On the other hand, the synthesis of derivatives substituted at the pyrrolidine ring has been less studied. In particular, specific polyhydroxylated pyrrolidinyl β-amino phosphonic acids have been synthesized from a cyclic imine [36], a nitrone [37], and amino sugars [38]. Based on our previous experience on nucleophilic additions to polyhydroxylated acyclic [39] and cyclic nitrones [40, 41], we envisioned nitrones **6** as suitable substrates for the addition of methylphosphonates **7**, a reaction that had been described in only one particular case [37]. Consequently, we started our study with a survey of nucleophilic additions of methylphosphonates to cyclic nitrones as a general synthetic approach for the synthesis of β-amino phosphonic acids.

2.1 | Synthesis of β-amino Phosphonates

Nitrones **6a–c** were prepared as reported [41]. Phosphonates **7a–d** were selected as nucleophiles; we considered different substitutions (methyl, ethyl, benzyl, allyl) to check the required deprotection of the phosphonate functionality for the further coupling with uridine monophosphate (UMP) **5**. While phosphonates **7a, b** are commercially available, compounds **7c** [42] and **7d** [43] were prepared as described. One equivalent of butyllithium was used for generating the phosphonate anion and the reaction was carried out in anhydrous tetrahydrofuran (THF) at −80°C in a similar way to that reported for other nucleophilic additions of organolithium compounds to nitrones [41, 44–46]. (Scheme 1). The reaction was completed in hours (see Table 1) and hydroxylamines **8–10** were obtained in good

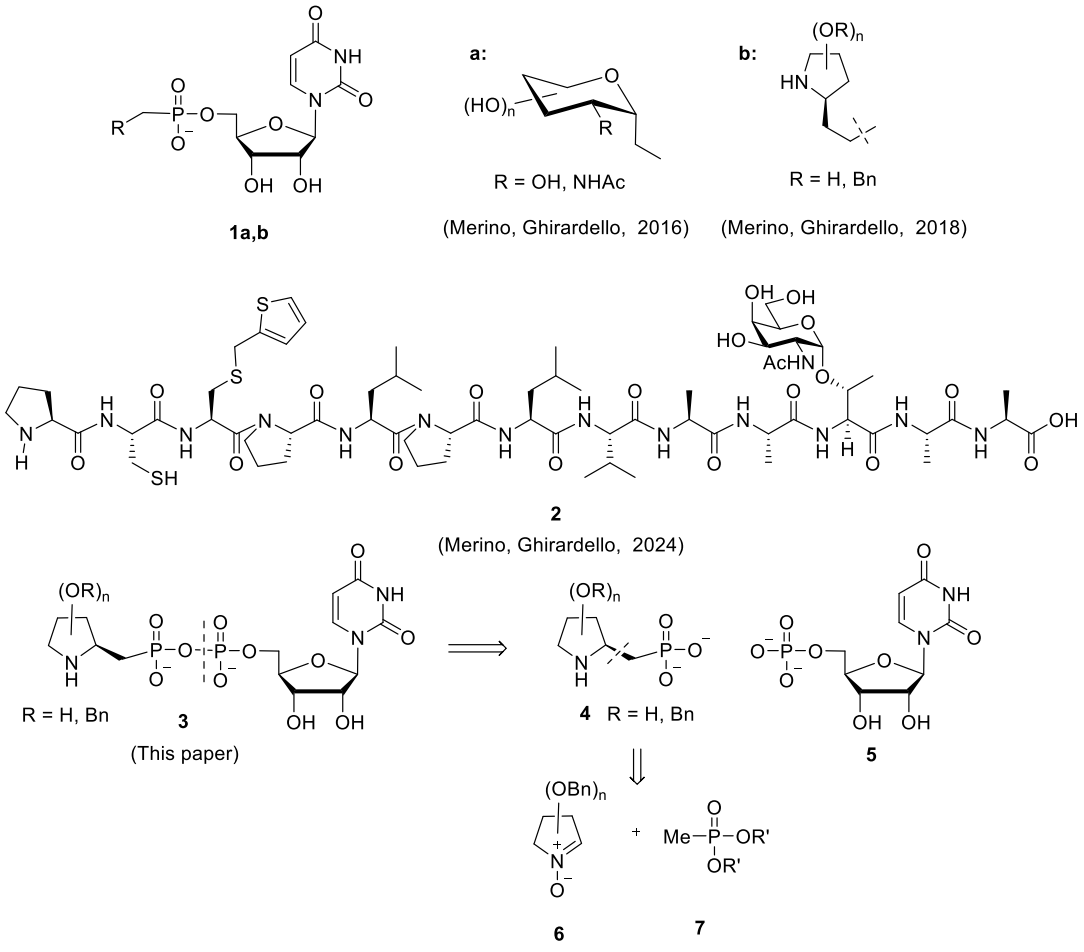

FIGURE 1 | Glycosyltransferase inhibitors and retrosynthetic analysis.

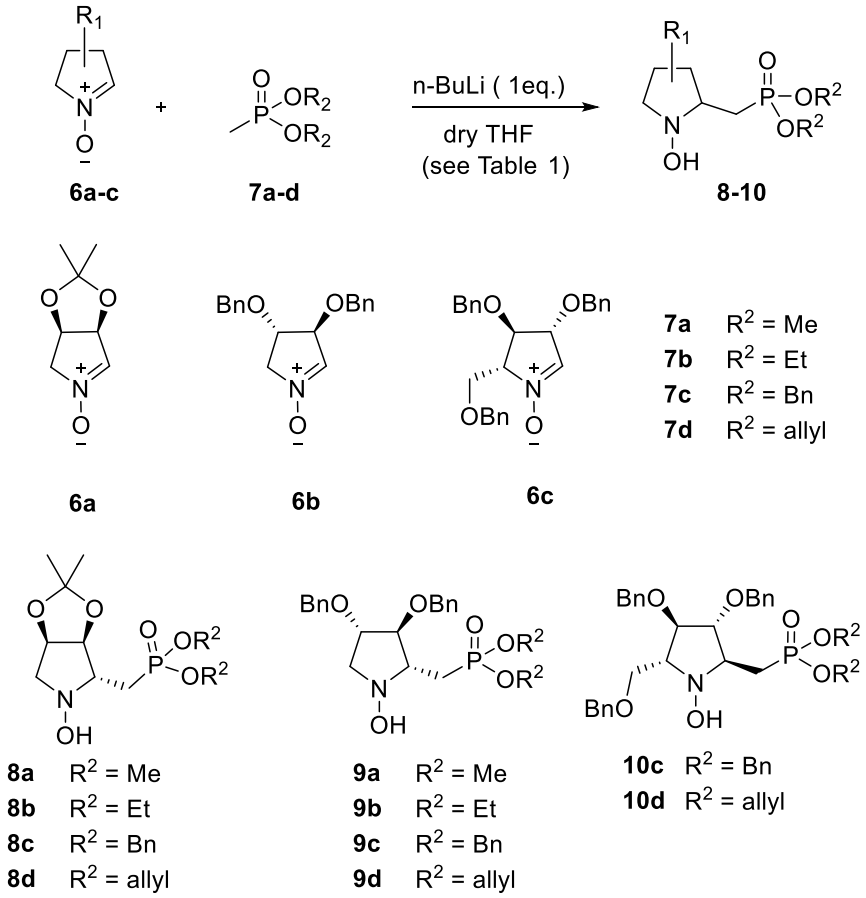

SCHEME 1 | Phosphonylation of cyclic nitrones (see Table 1).

TABLE 1 | Phosphonylation of cyclic nitrones (see Scheme 1).

Entry	6	7	T, °C	t, h	8–10	Yield, %[a]	d.r.[b]
1	**6a**	**7a**	−80	2	**8a**	95	>95:5
2	**6a**	**7b**	−80	1	**8b**	97	>95:5
3	**6a**	**7c**	−80	1	**8c**	95	>95:5
4	**6a**	**7d**	−80	3	**8d**	96	>95:5
5	**6b**	**7a**	−80	2	**9a**	96	70:30
6	**6b**	**7b**	−80	2	**9b**	89	70:30
7	**6b**	**7c**	−80	2	**9c**	96	75:25
8	**6b**	**7d**	−80	3	**9d**	92	75:25
9	**6c**	**7c**	−80	4	**10c**	96	75:25
10	**6c**	**7d**	−80	12	**10d**	97	78:22

[a]After isolation by column chromatography.
[b]Determined by ^{1}H-RMN from the crude product.

isolated yields. Whereas hydroxylamines obtained from **6a** were obtained as an only diastereomer, those derived from nitrones **6b** and **6c** showed a moderate *trans* selectivity with respect to the α-substituent (Scheme 1, Table 1). Nitrone **6c** required longer reaction times probably due to a higher steric hindrance. The stereochemistry of the addition of organolithium reagents and Grignard reagents can be controlled in the case of acyclic nitrones (which exhibit a Z configuration), as we have extensively demonstrated in the past [39]. In cyclic nitrones, which are more reactive due to their E configuration and have a clearly more accessible diastereoface, such stereocontrol is not evident because these systems are practically planar, unlike their acyclic counterparts. Nevertheless, in 2010 we reported that some degree of stereocontrol in the addition of Grignard reagents to cyclic nitrones was possible [41]. By adjusting the temperature and using specific Lewis acids, certain conformational changes in the starting complexes, showing similar barriers to those of the reaction itself, forced the reaction to proceed preferentially through the apparently more hindered face. With this background, we conducted several experiments by adding reagent **7a** to nitrones **6** in the presence of Lewis acids such as BF_3 or Et_2AlCl at various temperatures. In all cases, these attempts were unsuccessful, and when the reaction was carried out at −80°C, the results were very similar to those obtained under the previously described conditions. At higher temperatures, the yields dropped drastically. This is very likely due to the much higher reactivity of the organolithium derivative (which already reacts at −80°C), whereas the Grignard reagent does not react (or reacts only very slowly) below −50°C which probably allows enough time for conformational equilibria to be established.

The relative 2,3-*trans* configuration of the major adduct was unequivocally determined by NMR (NOESY experiments; see Supplementary Information (SI)). That configuration is in agreement with a steric course of the reaction, in which the nucleophile enters by the less hindered face with respect to the α-substituent. In the case of nitrones **6b** and **6c**, the presence of substituents on both faces contributes to the lower diastereoselectivity observed.

Nevertheless, the major product is obtained through attack on the face opposite to the substituent adjacent to the reactive center.

2.2 | Computational Density Functional Theory Studies

We carried out density functional theory (DFT) calculations at wb97xd/def2svp//wb97/def2tzvp/SMD = THF level of theory and also checked the b3lyp-3dbj functional using Grimme's empirical correction (see SI). The phosphonylation reaction of nitrones **6a–c** with the lithium derivative **EP** (obtained from **7a**) was carried out, using in the case of nitrones **6b,c** the analogs bearing a methyl group instead of a benzyl group. Since the benzyl group can orient itself in such a way that the two hydrogens of the methylene group point toward the area of greater steric hindrance, thus exerting an effect very similar to that of a methyl group, this substitution is considered a valid model that avoids excessively high conformational variability in the transition structures. In the reaction of nitrones **N1–3** with **EP**, the formation of an encounter pair **EPa–c** was observed, corresponding to the coordination of the nitrone oxygen atom with the metal, from which the addition could occur on two diastereotopic faces, *Re* and *Si*, with respect to the nitrone carbon (Scheme 2).

The chelate formed by the oxygen atoms bonded to phosphorus and nitrogen determines the geometry of the addition, which has practically no conformational variability beyond what the five-membered ring can provide, and this is limited, as the ring participates in the addition and contains a double bond. In the case of nitrone **N1**, the two diastereofaces are clearly differentiated by the presence of the cyclic acetal on one of them, which makes addition through this face much less favorable. The 5.2 kcal/mol difference between the two possible transition structures perfectly reflects the experimental result, in which only the adduct arising from attack on the less hindered face (the *Si* face) is observed.

By contrast, in the case of nitrones **N2** and **N3**, the presence of substituents on both faces results in a much lower diastereoselectivity, although a certain directing effect of the group adjacent to the reactive center can still be observed. This is reflected in the small energy differences between the two possible transition structures, which, in the case of nitrone **N2**, disappear when the wb97xd functional is used. For nitrone **N3**, a similar situation is observed, since the calculated differences are below 1 kcal/mol. On the basis of these results, it can be concluded that the calculations correctly predict the trend of the additions, clearly distinguishing between nitrone **N1** and nitrones **N2** and **N3**. Because the energy differences for the latter fall within the experimental error [47], only the formation of mixtures of diastereomers can be predicted, as is indeed observed experimentally. Figure 2 shows the optimized geometries of the transition-state structures for each nitrone and their relative energy values. The activation energies, both from the corresponding encounter complex and from the reactants themselves, correlate well with the observed reactivity, falling in the range between 6 and 8 kcal/mol (see SI).

2.3 | Synthesis of Nucleotide Analogs

The corresponding free β-aminophosphonic acids **4** are necessary to carry out the coupling with UMP. Several possibilities are available from the different hydroxylamines prepared having different alkoxy groups at the phosphorous atoms. After several attempts of deprotecting hydroxylamines **8–10**, the methyl (**a** series) and ethyl (**b** series) derivatives were discarded due to the low overall yield

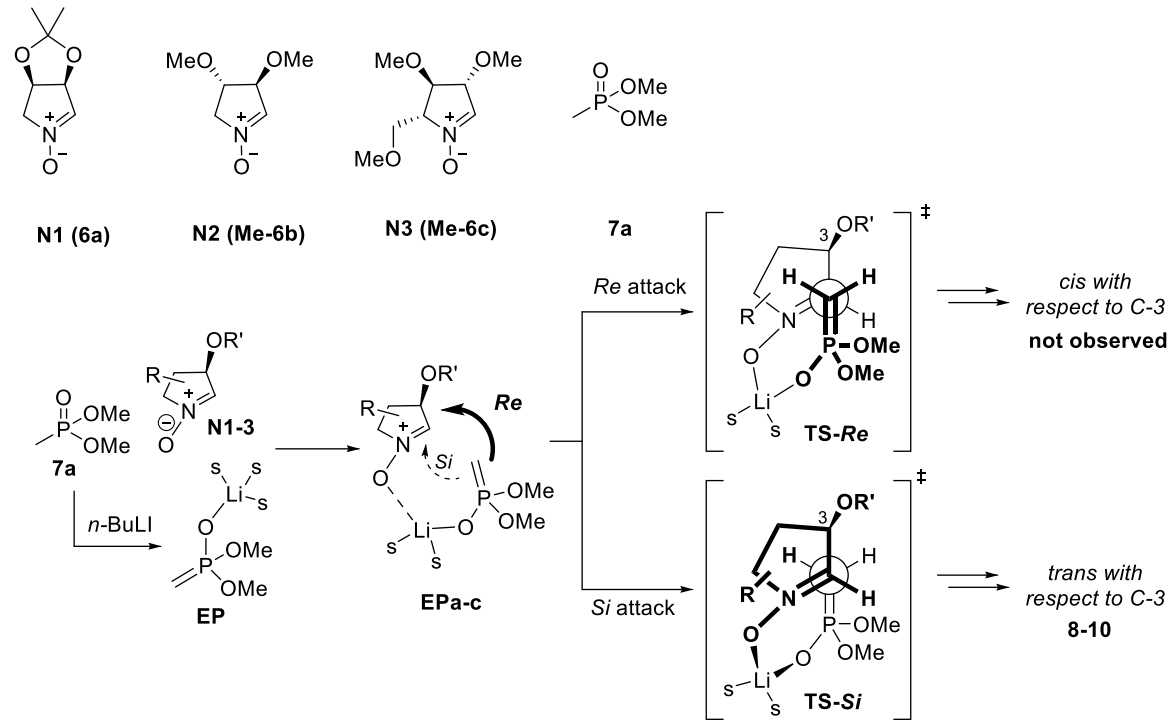

SCHEME 2 | DFT calculations of the addition of **N1-3** to compound **7a.** Lithium is considered tetrahedral and discrete solvent molecules (THF) are added at convenience. DFT = Density functional theory.

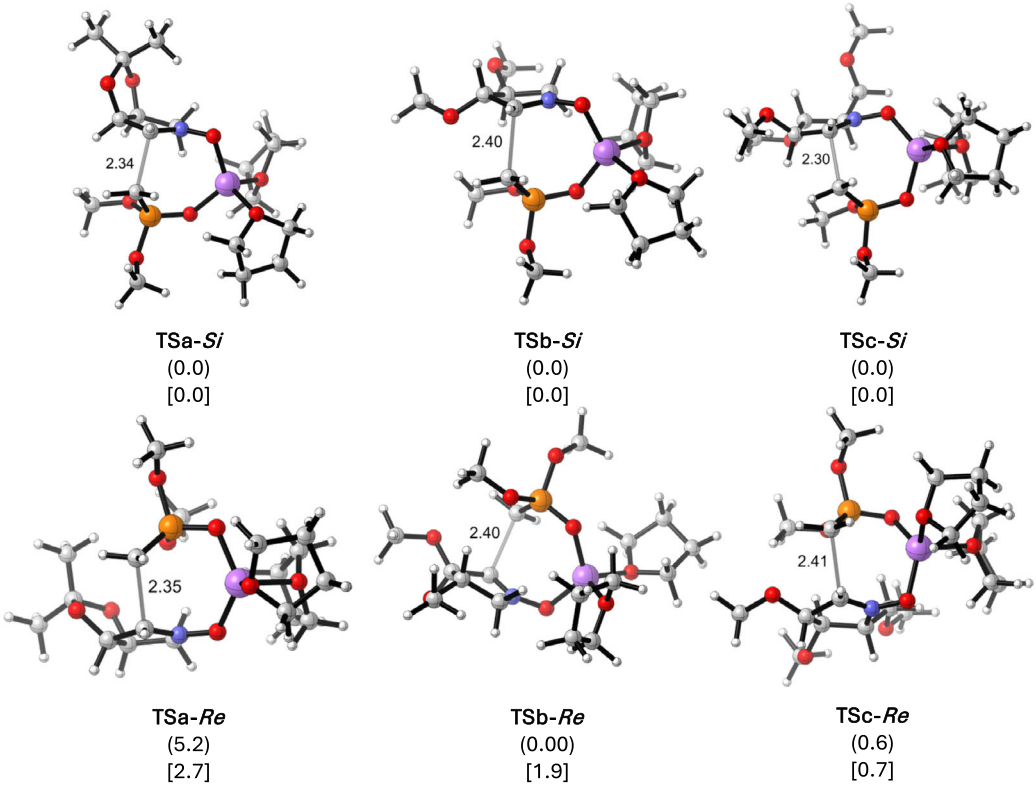

FIGURE 2 | Optimized (wb97xd/def2svp/smd=THF) geometries of the transition structures corresponding to the addition of **EP** (obtained from **7a**) to nitrones **N1 (TSa), N2(TSb) N3 (TSc)** through the two different diastereofaces. Relative energies are given in kcal/mol. Values in parentheses correspond to the wb97xd/def2tzvp/smd=THF level of theory. Values in square brackets correspond to the b3lyp-gd3bj/def2tzvp/smd=THF. Explicit THF molecules are introduced to complete lithium tetrahedral coordination.

obtained during the deprotection procedures. On the other hand, the catalytic hydrogenation of benzyl derivatives (**c** series) using palladium on carbon, and in the presence of hydrochloric acid in the case of compound **8c**, leads to the corresponding totally unprotected phosphonic acids **4a–c** (Scheme 3).

The reduction of allyl derivatives (**d** series) yields pyrrolidines **11a–c** in excellent yields. Further deprotection of the allyl group was attempted with dimedone in the presence of $Pd(PPh_3)_4$ [48, 49], and although the allyl group was removed the product was contaminated with dimedone. The deprotection of the allyl group was carried out with potassium hexachloroplatinate (IV); however, the reaction required stoichiometric amounts of metal complex, resulting in the contamination of the product by platinum. Finally, the deprotection with a catalytic amount of palladium dichloride in a mixture of dichloromethane/methanol as a solvent [50] yields partially protected (in the pyrrolidine ring) β-phosphonic acids **4d-f** (Scheme 3). The obtained phosphonic acids were isolated and utilized without further purification. Hydrogenation of these derivatives as described above yielded **4a–c**.

UMP was alternatively activated with morpholine and imidazole to yield the corresponding intermediates **13** and **14**, respectively. Coupling reaction between β-aminophosphonic acids **4a–f** as bis(triethylammonium) salts and UMP activated as imidazolate [51, 52] **14** (which showed the best results) produces the nucleotide analogs **3a–f** (Scheme 4). Purification of compounds **3a–c** proved very complicated due to the presence of UMP dimer formed during the coupling, which required longer times that in the case of totally unprotected compounds. Only by using buffer of ammonium formate at pH = 4, the dimer could be separated by high-performance liquid chromatography (HPLC), but under those conditions, compounds **3a, b** were obtained partially hydrolyzed and could not be characterized.

2.4 | Binding Studies

Compounds **3a,d–f** were subjected to enzyme-binding studies to human GalNAc-T2 using microscale thermophoresis and compared with UDP. Prior to the binding experiments, the enzyme was labeled with reactive dyes using *N*-hydroxysuccinimide–ester chemistry, which reacts efficiently with the primary amines of proteins to form highly stable dye–protein conjugates. All experiments were conducted in binding buffer (50 mM HEPES pH 7.5) using a constant concentration of the enzyme (5 nM) and serial dilutions of each ligand (for details, see SI). Dissociation constants (K_d) were calculated using MO affinity analysis (Table 2).

The high value observed for compounds **3a** and **3d** suggests the necessity of aromatic rings in the ligand. Only compound **3e** showed a higher affinity than UDP (4.68 μM vs 61.94 μM). As expected, this value was higher than those observed for other pyrrolidinyl derivatives previously reported [29] in which the β-phosphate had been replaced by an alkyl chain. In this case, since the nucleotide is the same, the comparison with UDP points out the enhanced affinity due to the pyrrolidinyl moiety as an additional anchorage point. The observed K_d value for **3e** suggests the presence of a hydrophobic pocket close to the active site in which the aromatic rings might accommodate. The

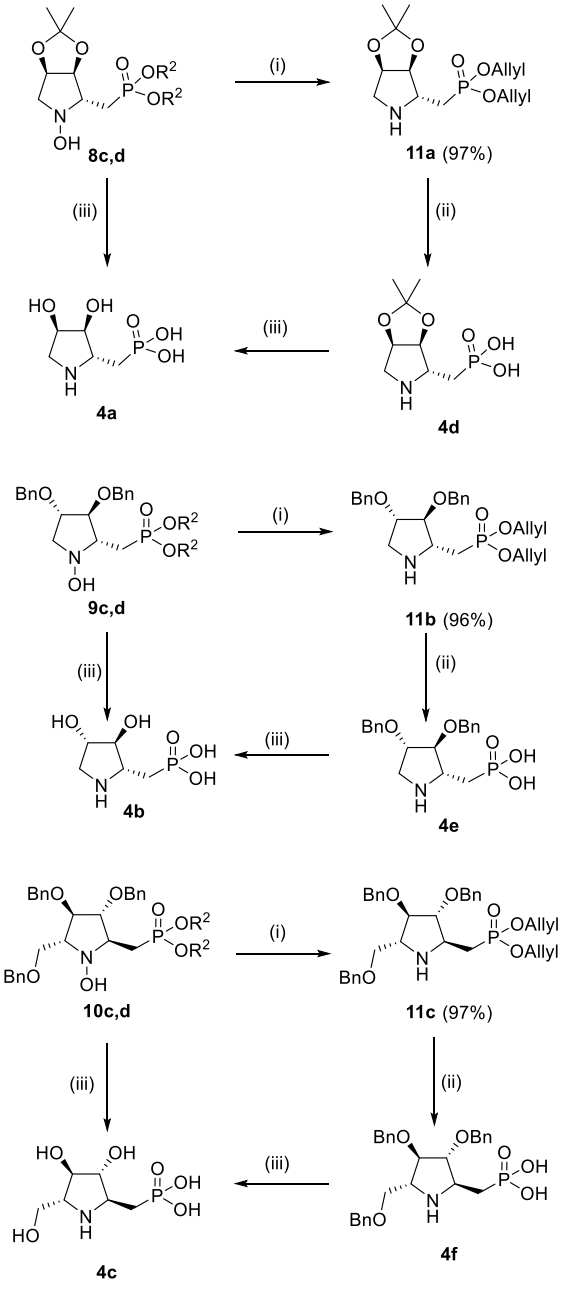

SCHEME 3 | Phosphonylation of cyclic nitrones (see Table 1). Preparation of pyrrolidinyl phosphonic acids. Reagents and conditions. (i) Zn, AcOH (aq) (series d, R^2 = allyl). (ii) $PdCl_2$, 2:3 Cl_2H_2/MeOH (iii) H_2, Pd–C; HC (10%) in MeOH (series c, R^2 = Bn).

observed difference with compound **3f**, with a dissociation constant ten times higher than **3e**, might be due to the presence of the third aromatic ring. However, this cannot be definitive due to the different stereochemical disposition of the benzyloxy groups at positions 3 and 4 of the pyrrolidine ring.

2.5 | Saturation Transfer Difference Nuclear Magnetic Resonance Studies

To shed some light about the recognition of **3e** by GalNAC-T2, we carried out STD-NMR experiments. STD-NMR spectroscopy [53, 54] has been demonstrated to be of great utility in evaluating ligand–protein binding affinities [55, 56] even in living cells [57, 58], and, particularly, with carbohydrates [59]. STD-NMR allows the identification of binding epitopes [60, 61], which reflect the distances between ligand protons and protons of binding site residues. More recently, imaging STD-NMR allows the detection of nonspecific binders by monitoring any variation in the binding epitope [62, 63]. STD-NMR experiments were carried out on **3e** and **3f**, for the purpose of comparison. UDP was selected as a reference. To obtain the epitope mappings of the selected ligands, UDP, **3e** and **3f** were incubated with GalNAc-T2 at pH 7.4 and the STD-NMR spectra were acquired at 25°C. Due to the low affinity, the experiments were carried out with a 1:50 enzyme/ligand ratio, which yielded STD spectra with the best quality. Analysis of the STD intensities allowed mapping of the epitopes of UMP and compounds **3d** and **3e** (Figure 3).

For compound **3f**, the STD spectrum showed signals corresponding to the phenyl groups and the nucleotide (H1′ and H6). In the case of compound **3e,** the same signals are observed but with higher intensity indicating a greater binding. In addition, a weak interaction can also be observed for H5. We also carried out a competence experiment between **3e** and UDP. When an excess of UDP was added to a mixture of 3e and GalNAc-T2, the new STD-NMR spectrum showed slightly diminished signals for **3e** and new signals corresponding to UDP confirm the competition of UDP and **3e** by the active site. These results suggest the presence of a hydrophobic pocket near the catalytic site, more specifically in the vicinity of the carbohydrate-binding region

2.6 | Docking and Molecular Dynamics Studies

We were also prompted to carry out computational studies to provide a 3D perspective of the GalNAc-T2/ligand complexes, accounting for the improved affinity observed for **3e** and to extend these studies to GalNAc-T14 [64] and GalNAc-T16 [65], which are known to perform related biological functions and also play an important role in the *O*-glycosylation of mucins [66]. GalNAc-T14 and GalNAc-T16, together with GalNAc-T2, form the phylogenetic subgroup Ib and share 53% and 49% sequence identity, respectively.

All GalNAc-Ts possess both a lectin domain and a catalytic domain (except for GalNAc-T20, which lacks the lectin domain), connected by a linker sequence that varies among isoforms and determines the two possible relative orientations of these domains [67]. These two different orientations, which are responsible for long-range prior glycosylation in alternative directions, are not always functional across all isoforms. Whereas GalNAc-T2 has been well characterized including extensive X-ray crystallography of both active and inactive conformations [68], no structural data are available for GalNAc-T14 or GalNAc-T16. Therefore, we employed deep learning-based methods [69] based on Alphafold 3 to obtain the corresponding structures (Figure 4). Notably, while GalNAc-T14 adopted the same relative orientation as GalNAc-T2, the T16 isoform exhibited a different orientation, even though the lectin and catalytic domains were individually superimposable. This result was not incompatible with the observed glycosylation patterns, and since our study focuses solely on interactions within the catalytic domain, MD simulations with compound **3e** were performed using the structures as obtained from Protenix.

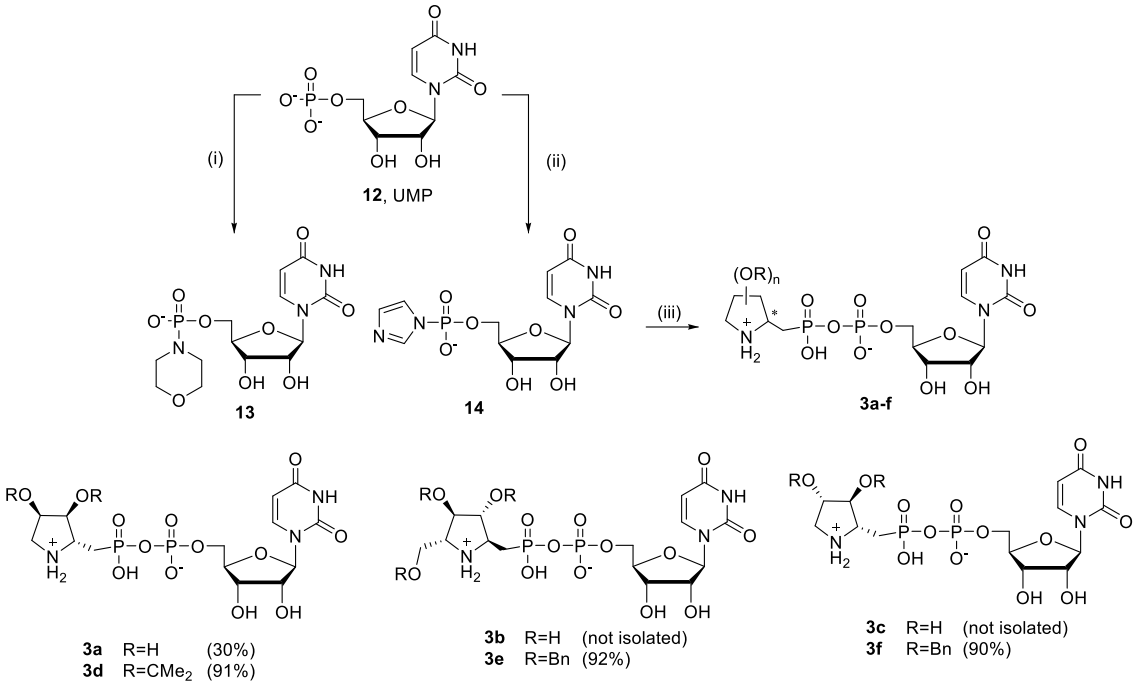

SCHEME 4 | Preparation of nucleotide analogs. (For **3a–f** see Chart 1). Reagents and solvents. (i) morpholine, dicyclohexylcarbodiimide, tert-butanol/water. (ii) imidazole, dithiopyridine, triethylphosphine, triethylamine, *N*, *N*-dimethylformamide. (iii) magnesium chloride, anhydrous *N*, *N*-dimethylformamide, **4a–f**.

TABLE 2 | Dissociation constants of compounds **3a,d–e** against GalNAc-T2.

Entry	Ligand	K_d
1	UDP	61.94 ± 26.5 μM
2	**3a**	981.51 ± 609 μM
3	**3d**	2.74 ± 1.83 mM
4	**3e**	4.68 ± 2.1 μM
5	**3f**	494.34 ± 224.06 μM

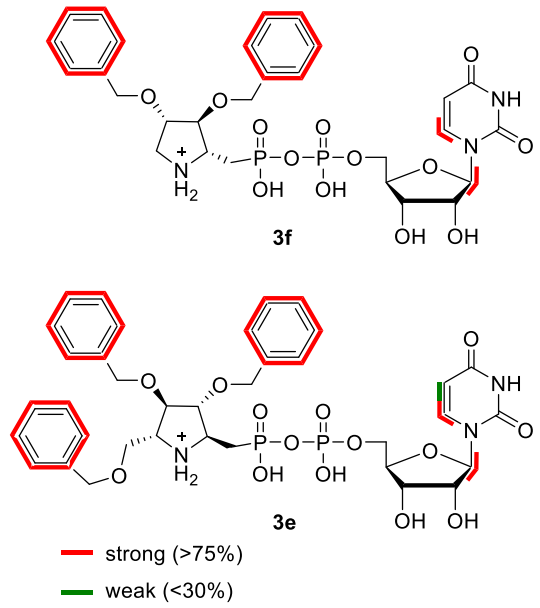

FIGURE 3 | Epitope mapping of compounds **3e** and **3f**.

Docking calculations of compound **3e** into GalNAc-T2 were initially performed using Glide [70, 71]. On the basis of the crystal structure of the active form of GalNAc-T2 (PDB ID: 4D0Z), we observed that the key interactions with the diphosphate moiety are preserved, including the hydrogen bonds with residues R362 and W331 (see the SI for details). Since no crystal structures are available for T14 or T16, an AI-based approach (Protenix) [69], recently developed for protein–ligand complex prediction, was applied instead of conventional docking. For comparison, the GalNAc-T2–**3e** complex was also predicted using this methodology, yielding results essentially identical to those obtained with Glide. The resulting complexes of T2, T14, and T16 with **3e** were subsequently used as starting structures for MD simulations to evaluate the stability of the protein–ligand interactions over time. Accordingly, we run 500 ns MD simulations in explicit water on the three complexes: GalNAc-T2 and **3e**; GalNAc-T16 and **3e**, and GalNAc-T16 and **3e**. The data revealed that the complex with GalNAc-T16 displayed larger changes with RMSD 7.18±2.3 Å as compared with the complexes with GalNAc-T2 (RMSD 3.69±0.51 Å) and GalNAc-T14 (RMSD 1.52±0.20 Å). The results of the MD simulations clearly show that the interactions with **3e** are almost entirely hydrophobic in nature.

In the active site of GalNAc-T2, residues Asp224 (catalytic base), Ser225, His226, and His359, considered essential for the catalysis, coordinate the metal and they are part of the conserved DxH motif typical of GTs from the GT27 family [72]. Residues Gly332, Arg208, Glu334, and Gly308 are responsible of specificity by forming

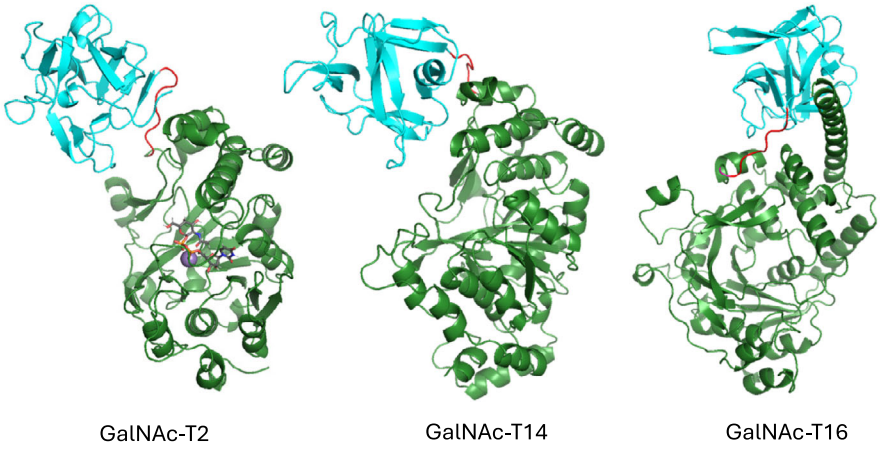

FIGURE 4 | X-ray structure (PDB ID: 4D0Z) of GalNAc-T2 and predicted (Alphafold 3) structures of GalNAc-T14 and GalNAc-T16. Lectin domain is showed in cyan; catalytic domain is showed in green; and peptide linker is showed in red. For GalNAc-T2 manganese is shown as a sphere in violet and UDP-GalNAc is shown in gray. PDB = Protein Data Bank.

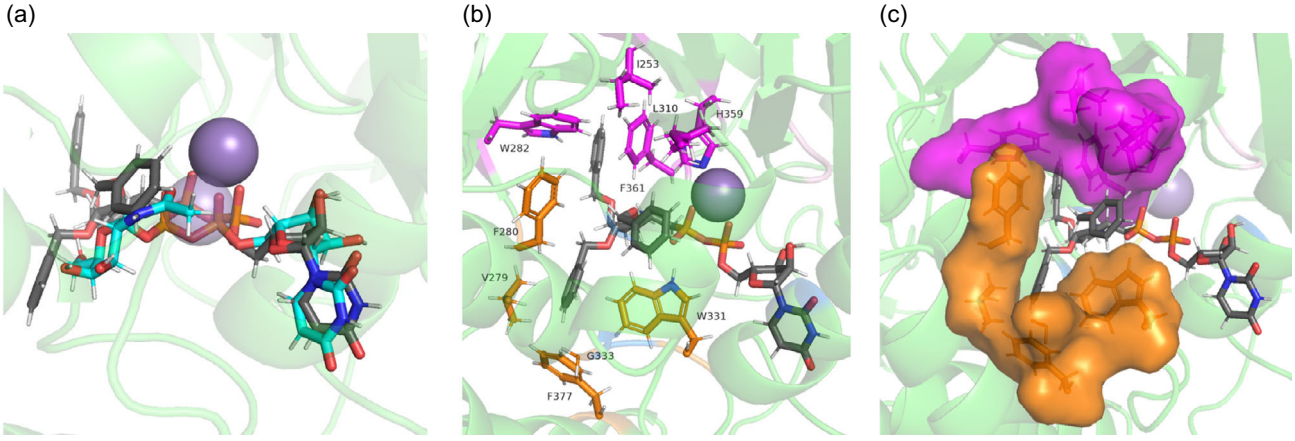

FIGURE 5 | (a) Overlay of UDP-GalNAc (cyan) coordinated to Mn^{+2} ion (PDB ID: 4D0Z) and compound **3e** (gray) in the complex with GalNAc-T2. (b,c) Detail of the two pockets (colored in orange and magenta) observed in the catalytic site and interactions with **3e** (gray). The corresponding surfaces are showed in (c). In all cases, the same orientation is shown. PDB = Protein Data Bank.

H-bonds; Arg362, Lys331, and Lys363 stabilize the pyrophosphate group and facilitate nucleotide binding and Val279, Phe280, Tyr367, and Phe377 form a secondary GalNAc-binding site [68]. Preliminary experiments with derivatives in which the pyrrolidine ring was substituted by an aromatic ring demonstrated that aromatic residues can accommodate in that binding pocket. These studies also revealed an additional hydrophobic pocket defined by Ile253, Trp282, Leu310, His359, and Ph361 [73]. Both hydrophobic pockets are conserved in GalNAc-T3, T4, T14, and T16 (main residues are shown in Figure 4).

Compound **3e** occupies the same position as UDP-GalNAc (Figure 5a); in fact, the nucleotide moiety is almost perfectly superimposable in both cases, which is consistent with the results obtained by STD-NMR. By contrast, the pyrophosphate group slightly deviates from the orientation observed in UDP-GalNAc, forming the only hydrogen bond that persists for more than 50% of the simulation. In contrast, the hydrophobic interactions of the aromatic rings of compound 3e within the two previously described pockets are maintained throughout 100% of the simulation (Figure 5b,c), thus demonstrating the type of interactions that keep compound **3e** bound to GalNAc-T12.

In the case of GalNAc-T12 and T14, a very similar situation is found since both hydrophobic pockets are essentially conserved (see SI).

3 | Conclusions

In conclusion, we have developed an efficient and general synthetic strategy for the preparation of pyrrolidinyl-modified nucleotide analogs in which the sugar moiety of natural Leloir donors is replaced by a polyhydroxylated pyrrolidine scaffold. The key step relies on the highly diastereoselective nucleophilic addition of organophosphonates to cyclic nitrones, a process that is well supported by detailed DFT calculations and provides access to enantiomerically pure β-aminophosphonic acid intermediates. Subsequent deprotection and coupling with activated UMP afforded a series of novel nucleotide analogs that could be evaluated as ligands of GalNAc transferases. Experimental binding studies revealed that among the synthesized compounds, derivative **3e** exhibits a remarkably high affinity for GalNAc-T2, with a dissociation constant of 4.68 μM, which is almost one order of

magnitude lower than that of the natural substrate UDP. This result demonstrates that the introduction of the pyrrolidinyl moiety can significantly enhance ligand–enzyme recognition. The comparison with previously reported analogs in which the β-phosphate was replaced by an aliphatic chain clearly indicates that the β-phosphate group plays a crucial and nonreplaceable role in stabilizing binding at the active site. Nevertheless, the pyrrolidinyl ring provides an additional anchoring element, giving rise to a synergistic effect between the β-phosphate and the nitrogen-containing scaffold, which is ultimately responsible for the enhanced affinity observed for **3e**. STD-NMR experiments further validated the binding mode of compound **3e**, revealing that both the nucleotide fragment and the aromatic substituents of the pyrrolidine unit participate directly in the interaction with GalNAc-T2. Competition experiments with UDP confirmed that **3e** binds at the catalytic site. These results provided direct experimental evidence for the relevance of hydrophobic contacts in addition to the canonical phosphate-driven electrostatic interactions.

MD simulations offered a detailed 3D picture of the molecular recognition process and fully rationalized the experimental data. Compound **3e** adopts essentially the same orientation as UDP-GalNAc within the catalytic pocket, with a nearly perfect superposition of the nucleotide moieties. While the pyrophosphate group shows a slight deviation from the natural substrate and forms only a limited number of persistent hydrogen bonds, the aromatic substituents of the pyrrolidinyl scaffold engage in strong and long-lived hydrophobic interactions within two conserved hydrophobic pockets of the enzyme. These interactions are maintained throughout the full simulation time and are also preserved in the closely related isoforms GalNAc-T14 and GalNAc-T16, highlighting the potential of this scaffold for the development of broad-spectrum GalNAc-T inhibitors. Altogether, this work demonstrates that polyhydroxylated pyrrolidinyl nucleotide analogs represent a valuable and versatile platform for the design of glycosyltransferase inhibitors. The combined synthetic, spectroscopic, and computational approach has allowed us to dissect the respective roles of the nucleotide, the β-phosphate, and the pyrrolidinyl unit in enzyme recognition. Ongoing efforts are currently directed toward (i) the identification of nonpolar substituents capable of partially replacing the β-phosphate while preserving key interactions, and (ii) the development of alternative sugar mimetics that may further improve affinity and selectivity toward GalNAc transferases. These advances are expected to contribute to the rational design of new chemical probes and potential therapeutic leads targeting mucin-type *O*-glycosylation.

4 | Experimental Section

4.1 | General Methods

Analytical grade solvents and commercially available reagents were used without further purification. Anhydrous solvents were purified and dried with activated molecular sieves prior to use. For reactions carried out under inert conditions, the argon was previously dried through a column of P_2O_5 and a column of KOH and $CaCl_2$. All the glassware was dried for 12 h prior to use in an oven at 140°C and allowed to cool under humidified atmosphere. For the removal of solvents under reduces pressure Büchi R-210 rotary evaporators were used. NMR: ^{1}H NMR, ^{13}C NMR, and ^{31}P NMR were acquired at 25°C on Bruker Avance 400 MHz or AVANCE II 300 MHz instruments in the stated solvent. Chemical shifts (δ) are reported in ppm relative to residual solvent signals and coupling constants (J) in hertz (Hz). NMR assignments were using standard 2D experiments. NMR assignments were made using the following general pattern.

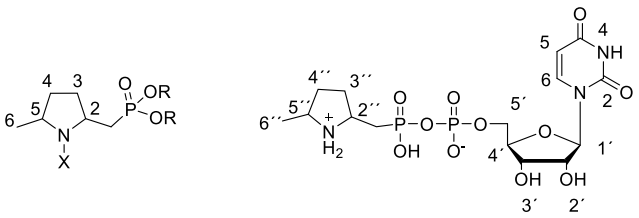

HPLC: Analytical: Column Atlantis dc18 5 µm, 4.6 × 100 mm. Semipreparative: (Column Atlantis dc18 OBD 5 µm, 19 × 100 mm) was carried out in a waters 515 pump with PDA detection. HRMS: High-resolution mass spectra (HRMS) were recorded on a QToF spectrometer equipped with an ESI (electrospray ionization) source (microTOF-Q, Bruker Daltonik) using sodium formate as external reference.

4.2 | General Procedure for the Preparation of ((1-Hydroxypyrrolidin-2-Yl) Methyl)phosphonates (8a–d, 9a–d, 10c,d)

To a well-stirred solution of the corresponding phosphonate (1.28 mmol) in anhydrous THF (3 mL) cooled to −78°C, under an argon atmosphere, *n*-BuLi (1.28 mmol) was added dropwise. After 10 min, a solution of the corresponding nitrone (0.64 mmol) in anhydrous THF (2 mL) was added dropwise. The reaction was monitored by TLC and kept at −78°C until disappearance of the nitrone. When the reaction is finished, saturated NH_4Cl solution (5 mL) was added. Then, the reaction was warm to room temperature and extracted with DCM (3x10 mL). The combined organic layers were dried with $MgSO_4$, filtrated, and then the solvent was removed under reduced pressure. The crude was purified by flash chromatography (gradient Hexane/EtOAc 80:20 to EtOAc).

4.3 | General Procedure to Obtain ((pyrrolidin-2-Yl) methyl)phosphonates (11a–c)

To a well-stirred solution of the corresponding *N*-hydroxypyrrolidine (1.50 mmol) in 5 mL of a mixture of H_2O/AcOH (1:1), Zn (3 mmol) was added. The mixture was vigorously stirred for 5 h at room temperature. When reaction is finished, it was diluted with water, basified with solid $NaHCO_3$ to pH = 9 and extracted with DCM (3 × 50 mL). The combined organic layers were dried with anhydrous $MgSO_4$ and concentrated under reduced pressure.

4.4 | General Procedure to Obtain ((pyrrolidin-2-Yl) methyl)phosphonic Acids (4a–c)

A stirred solution of the corresponding phosphonate (8–10c) (0.60 mmol) in MeOH (4 mL) was treated with Pd/C (10 mol%) and stirred at room temperature for 3 days under an hydrogen atmosphere (25 mbar). When reaction is finished, controlling by NMR, it was filtered through a Celite pad and methanol was

remove under reduced pressure to give the corresponding phosphonic acid (4a–c) which were used without further purification.

4.5 | General Procedure to Obtained ((pyrrolidin-2-Yl)methyl)phosphonic Acids (4d–f)

To a stirred solution of the corresponding pyrrolidinyl phosphonate (**11a–c**) (1.40 mmol) in DCM/MeOH (2:3), $PdCl_2$ (0.7 mmol) was added. The reaction was stirred at room temperature 18hr under argon atmosphere. When the reaction is finished, it was filtered through Celite and washed with MeOH. After that, the solution was stirred 2 hr with scavengers (Quadra Pure TU), to eliminate possible remains of palladium. The resulting mixture was filtrated and the solvent evaporated under reduced pressure to afford the corresponding phosphonic acids as crude product.

4.6 | General Procedure to Obtain Compounds 3a–f

The corresponding ((pyrrolidin-2-yl)methyl)phosphonic acids (**4a–f**) as triethylammonium salt (0.20 mmol) and $MgCl_2$ (0.40 mmol) were vigorously stirred in dry DMF (1.5 mL) until clear solution was obtained. To this mixture was then added a solution of **14** (0.26 mmol) in anhydrous DMF (1.5 mL) under argon. This reaction mixture was stirred for several days at room temperature, and the reaction progress was monitored by ^{31}P-NMR. The reaction was quenched by the addition of water (10 mL, HPLC grade). The solvents were removed under pressure and the crude was purified using semipreparative HPLC.

4.7 | Computational Methods

4.7.1 | Density Functional Theory Calculations

All the calculations were performed using the Gaussian16 program [74]. Computations were done using wb97xd [75] functional in conjunction with standard basis sets def2SVP and def2TZVP [76, 77]. Geometry full optimizations were made at wb97xd/def2SVP level. Single-point calculations using def2TZVP basis set were carried out over optimized geometries to obtain the energy values. Solvent effects (THF) were considered using the SMD model [78]. The thermal and entropic contributions to the free energies were also obtained from the vibrational frequency calculations, using the unscaled frequencies. Correction to free energy was made by substracing S_{trans} contribution and considering a 1 M concentration [79]. Structural representations were generated using CYLView [80]. (For more information, see SI.)

4.7.2 | Protein Models

UDP-GalNAc and the active conformation of the flexible loop were taken from PDB ID: 4D0T. Ternary complex of GalNAc-T2 with a peptide and UDP-5SGalNAc was taken from PDB ID: 4D0Z. Inactive forms have been taken from PDB IDs: 5AJN, 5AJO and 5AJP. The amino acid sequences of the proteins GalNAc-T14 (UniProt ID: Q96FL9) and GalNAc-T16 (UniProt ID: Q8N428) were modeled. Software Protenix [69] based on AlphaFold [81] (ref. https://doi.org/10.1038/s41586-024-07487-w) was used to produce 3D models of GALNT14 and GALNT16 in complex with Mn2+ and UDP-GalNAc. Per-residue pLDDT (predicted Local Distance Difference Test) score, measure of confidence in the local structure (https://doi.org/10.1093/bioinformatics/btt473) was used to estimate the reliability of the predicted models. Both GALNT14 and GALNT16 complexes showed pLDDT values of 85% and 86%, respectively, which lie near the highest confidence category (>90%) and assure the integrity of following calculations using these models.

The sequence was submitted in FASTA format, and five refinement cycles with energy minimization were applied to optimize the predicted structures. The above-mentioned experimentally determined structures from the Protein Data Bank (PDB) were used as references for structural comparison. Structural alignment between Protenix-generated models and the PDB structures was carried out using TM-align and PyMOL, calculating RMSD and TM-score to assess structural similarity. The stereochemical quality of the models was evaluated using MolProbity and Ramachandran plot statistics. Additionally, secondary structure elements, conserved residues, and active site features were compared across the predicted and experimental structures using UCSF.

4.7.3 | Molecular Docking

Water molecules, sulfate ions, *N*-acetylglucosamine, and ligands were removed from the model. In a second model, UDP-GalNAc was conserved. The protein was preprocessed by assigning bond orders, adding hydrogens, creating disulfide bonds and adding cap termini. The orientations of the hydroxyl groups from the Ser, Thr, and Tyr, the sulfhydryl protons of Cys, and methyl protons of Met were optimized. The positions of the hydrogen atoms on the histidine, asparagine, and glutamine residues were assigned to ensure the correct ionization states using Epik. Then, the protein was optimized with OPLS2005e force field [82]. We applied this procedure to all the protein models. Compounds were docked into the binding sites using Glide with the enzyme treated rigidly [71]. Grid was prepared with a box size of $25 \times 25 \times 25$ Å, centered on the corresponding binding site, using OPLS2005 force field. Conformational preparation of ligands started from the corresponding chair of the piperidine ring with the long chain at the nitrogen atom in an equatorial orientation. Glide was run on XP mode (Extra Precision), using as input the structures restraining nitrogen inversion and conformations to keep the chair orientation. The Glide score and the Prime energy of the poses were used to rank the final set of protein−ligand poses for each couple ligand-binding site.

4.7.4 | Molecular Dynamics Simulations

MD simulations were carried out with AMBER20 suite of programs [83]. Parameters for ligands **1–3** were generated with the antechamber module using the general Amber force field (GAFF2) [84], with partial charges calculated using AM1-BCC method. The ff14 SB force field [85] was employed to properly model the protein. The protein, together with the corresponding ligand, was neutralized and immersed in a water box with a 12 Å buffer of TIP3P [86] water molecules. A two-stage geometry optimization approach was carried out. i) Minimization of only the positions of solvent molecules was executed by 500 cycles of steepest descent minimization, followed by 500 cycles of conjugate gradient minimization, and (ii) unrestrained minimization of all the atoms in the simulation cell was executed by 2500 cycles

of steepest descent minimization, followed by 2500 cycles of conjugate gradient minimization. After system optimization, running of MD simulations was started on the systems by gradually heating each system in the NVT ensemble from 0 to 300 K for 100 ps using a Langevin thermostat with a coupling coefficient of 1.0/ps. Harmonic restraints of 10 kcal·mol-1 were applied to the solute, and the Langevin temperature coupling scheme [87] was used to control and equalize the temperature. The time step was kept at 2 fs during the heating stages, allowing potential inhomogeneities to self-adjust. Water molecules are treated with the SHAKE algorithm, such that the angle between the hydrogen atoms is kept fixed. Long-range electrostatic effects are modeled using the particle-mesh-Ewald method [88]. Then, 100 ps of density equilibration with a force constant of 2.0 kcal/mol·Å^2 on the complex was performed by releasing all the restraints. Finally, production trajectories were then run for 1 microsecond under the same simulation conditions. Pymol 2.0[1] was used for structural alignments and visualizations. During all MD simulations, replicated 3–5 times to ensure feasibility.

Author Contributions

Pedro Merino: investigation (lead), software (lead), supervision (lead), writing – original draft (lead), writing – review and editing (lead). **Veronica Juste:** methodology (equal). **Alejandro Montesa:** methodology (equal), software (lead). **Sandra Pereira:** methodology (supporting). **Sara Orta:** methodology (supporting). **Manuel Pedrón:** methodology (supporting), software (supporting). **Ana I. Jiménez:** conceptualization (supporting). **Sonsoles Martín-Santamaría:** investigation (supporting). **Ramón Hurtado-Guerrero:** conceptualization (lead), investigation (lead). **Ignacio Delso:** Synthesis and NMR experiments. **Tomás Tejero:** conceptualization (equal), project administration (lead), supervision (equal), visualization (equal).

Acknowledgments

We thank Ministerio de Ciencia e Innovacion (MICINN, Spain) (Projects PID2022-137973NB-I00 and PID2019-104090RB-I00 to P.M.; PID2022-136362NB-I00 to R.H.-G. and PID2020-113588RB-I00 and PID2023-152271NB-I00 to S.M.-S.) and Government of Aragón (Spain) (Grupos Consolidados, E34_20R) for financial support. V.J. and S.P. thank also MICINN for FPI predoctoral contracts. A.M., M.P., and S.O. thank Government of Aragon for predoctoral contracts. The authors thankfully acknowledge the resources from the supercomputers "Memento" and "Cierzo," technical expertise, and assistance provided by BIFI-ZCAM (Universidad de Zaragoza, Spain).

Funding

This work was supported by Ministerio de Ciencia e Innovación (grants PID2022-137973NB-I00, PID2019-104090RB-100, PID2022-136362NB-I00, PID2020-113588RB-I00, PID2023-152271NB-I00).

Conflicts of Interest

The authors declare no conflicts of interest.

Data Availability Statement

The data that support the findings of this study are available in the supplementary material of this article.

Endnotes

[1] The PyMOL Molecular Graphics System, Version 2.0 Schrödinger, LLC.

References

1. Y. Rossez, R. Leonard, O. Vidal, et al., "Mucins and Bacterial Interactions," *Methods in Molecular Biology* 2942 (2025): 177–186.

2. M. A. McGuckin and D. J. Thornton, *Methods in Molecular Biology*, 1st ed. (Springer, 2012). 342.

3. Y. Kang, H. Park, B. H. Choe, and B. Kang, "The Role and Function of Mucins and Its Relationship to Inflammatory Bowel Disease," *Frontiers in Medicine* 9 (2022): 848344.

4. P. Montero, I. Roger, J. Milara, and J. Cortijo, "Immunomodulatory Properties of Transmembrane Mucins: From Chronic Diseases to Cancer," *Physiological Reviews* 105 (2025): 2233–2304.

5. P. Argueso, "Human Ocular Mucins: The Endowed Guardians of Sight," *Advanced Drug Delivery Reviews* 180 (2022): 114074.

6. T. Breugelmans, B. Oosterlinck, W. Arras, et al., "The Role of Mucins in Gastrointestinal Barrier Function during Health and Disease," *The Lancet Gastroenterology & Hepatology* 7 (2022): 455–471.

7. I. Sanz-Martinez, S. Pereira, P. Merino, F. Corzana, and R. Hurtado-Guerrero, "Molecular Recognition of GalNAc in Mucin-Type O-Glycosylation," *Accounts of Chemical Research* 56 (2023): 548–560.

8. J. Chia, G. Goh, and F. Bard, "Short O-GalNAc Glycans: Regulation and Role in Tumor Development and Clinical Perspectives," *Biochimica Et Biophysica Acta (BBA)-General Subjects* 1860 (2016): 1623–1639.

9. Y. Wang, H. Zhang, W. Shi, et al., "High Soluble Expression and Characterization of Human GalNAc Transferase T2 and T11 in Escherichia Coli," *Protein Expression and Purification* 231 (2025): 106712.

10. V. Taleb, Q. Liao, Y. Narimatsu, et al., "Structural and Mechanistic Insights into the Cleavage of Clustered O-Glycan Patches-Containing Glycoproteins by Mucinases of the Human Gut," *Nature Communications* 13 (2022): 4324.

11. D. T. Tran, L. Zhang, Y. Zhang, E. Tian, L. A. Earl, and K. G. Ten Hagen, "Multiple Members of the UDP-GalNAc: Polypeptide N-Acetylgalactosaminyltransferase Family Are Essential for Viability in Drosophila," *The Journal of Biological Chemistry* 287 (2012): 5243–5252.

12. Q. Li, K. Yin, H. P. Ma, et al., "Application of Improved GalNAc Conjugation in Development of Cost-Effective siRNA Therapies Targeting Cardiovascular Diseases," *Molecular Therapy* 32 (2024): 637–645.

13. M. Tenno, "Analyzing Physiological Function of Polypeptide GalNAcT-1-Deficient Mice in Humoral Immunity," *Methods in Enzymology* 479 (2010): 173–184.

14. C. R. C. Verzijl, F. Oldoni, N. Loaiza, et al., "A Novel Role for GalNAc-T2 Dependent Glycosylation in Energy Homeostasis," *Molecular Metabolism* 60 (2022): 101472.

15. A. Pirillo, M. Svecla, A. L. Catapano, A. G. Holleboom, and G. D. Norata, "Impact of Protein Glycosylation on Lipoprotein Metabolism and Atherosclerosis," *Cardiovascular Research* 117 (2021): 1033–1045.

16. K. Akasaka-Manya, M. kawamura, H. Tsumoto, et al., "Excess APP O-Glycosylation by GalNAc-T6 Decreases Aβ Production," *Journal of Biochemistry* 161 (2017): 99–111.

17. S. Yue, X. Wang, W. Ge, et al., "Deciphering Protein O-GalNAcylation: Method Development and Disease Implication," *ACS Omega* 8 (2023): 19223–19236.

18. K. Lavrsen, S. Dabelsteen, S. Y. Vakhrushev, et al., "De Novo Expression of Human Polypeptide N-Acetylgalactosaminyltransferase 6 (GalNAc-T6) in Colon Adenocarcinoma Inhibits the Differentiation of Colonic Epithelium," *The Journal of Biological Chemistry* 293 (2018): 1298–1314.

19. A. Tsuchida, A. Matsuda, A. Tsuchida, et al., "Roles of GalNAc-Disialyl Lactotetraosyl Antigens in Renal Cancer Cells," *Scientific Reports* 8 (2018): 7017.

20. X. Dong, Z. Luo, Y. Wang, et al., "Altered O-Glycosylation Is Associated with Inherent Radioresistance and malignancy of Human Laryngeal Carcinoma," *Experimental Cell Research* 362 (2018): 302–310.

21. H. O. Duarte, D. Freitas, C. Gomes, J. Gomes, A. Magalhaes, and C. A. Reis, "Mucin-Type O-Glycosylation in Gastric Carcinogenesis," *Biomolecules* 6 (2016): 33/31–33/19.

22. B. A. Symmes, A. L. Stefanski, C. M. Magin, and C. M. Evans, "Role of Mucins in Lung Homeostasis: Regulated Expression and Biosynthesis in Health and Disease," *Biochemical Society Transactions* 46 (2018): 707–719.

23. S. Wang and S. Vidal, "Recent Design of Glycosyltransferase Inhibitors," *Carbohydrate Chemistry* 39 (2013): 78–101.

24. L. Tedaldi and G. K. Wagner, "Beyond Substrate Analogues: New Inhibitor Chemotypes for Glycosyltransferases," *MedChemComm* 5 (2014): 1106–1125.

25. H. C. Hang, C. Yu, K. G. Ten Hagen, et al., "Small Molecule Inhibitors of Mucin-Type O-Linked Glycosylation From a Uridine-Based Library," *Chemistry & Biology* 11 (2004): 337–345.

26. F. Liu, K. Xu, Z. Xu, et al., "The Small Molecule Luteolin Inhibits N-Acetyl-α-Galactosaminyltransferases and Reduces Mucin-Type O-Glycosylation of Amyloid Precursor Protein," *The Journal of Biological Chemistry* 292 (2017): 21304–21319.

27. M. Ghirardello, M. de las Rivas, A. Lacetera, et al., "Glycomimetics Targeting Glycosyltransferases: Synthetic, Computational and Structural Studies of Less-Polar Conjugates," *Chemistry–A European Journal* 22 (2016): 7215–7224.

28. I. Compañón, C. J. Ballard, E. Lira-Navarrete, et al., "Rational Design of Dual-Domain Binding Inhibitors for Nacetylgalactosamine Transferase 2 with Improved Selectivity Over the T1 and T3 Isoforms," *Journal of the American Chemical Society* 4 (2024): 3649–3656.

29. M. Ghirardello, D. Perrone, N. Chinaglia, et al., "UDP-GlcNAc Analogs as Inhibitors of O-GlcNAc Transferase (OGT): Spectroscopic, Computational and Biological Studies," *Chemistry–A European Journal* 24 (2018): 7264–7272.

30. O. Lopez, P. Merino-Montiel, S. Martos, and A. Gonzalez-Benjumea, "Glycosidase Inhibitors: Versatile Tools in Glycobiology," *Carbohydrate Chemistry* 38 (2012): 215–262.

31. N. T. Subasi, H. Yalcinkaya, and A. S. Demir, "Highly Selective Intermolecular One-Pot Three Component 1,3-Dipolar Cycloaddition Reaction of Aldehydes with Phosphonates and Proline," *Tetrahedron* 73 (2017): 4329–4334.

32. G. Li, M. Wu, D. Kong, R. Liu, X. Zhou, and F. Liu, "One-Pot and Highly Regio-Selective 1,3-Dipole Cycloaddition of Azomethine Ylide Generated In Situ to Tetraethyl Vinylidenebisphosphonate (VBP) Catalyzed by Cerium(IV) Oxide," *New Journal of Chemistry* 38 (2014): 3350–3353.

33. O. O. Kolodyazhnaya and O. I. Kolodyazhnyi, "Pyridinium Perchlorate: A New Catalyst for the Reaction of Trialkyl Phosphites with the C=X Electrophiles," *Russian Journal of General Chemistry* 81 (2011): 307–314.

34. T. Widianti, Y. Hiraga, S. Kojima, and M. Abe, "Novel Cyclic β-Aminophosphonate Derivatives as Efficient Organocatalysts for the Asymmetric Michael Addition Reactions of Ketones to Nitrostyrenes," *Tetrahedron Asymm* 21 (2010): 1861–1868.

35. K. Pachamuthu and R. R. Schmidt, "Straightforward Synthesis of Gem-Phosphonate-Phosphate Containing Compounds via One-Pot Reaction of Thioesters with Diethyl Phosphite," *Chemical Communications* (2004): 1078–1079.

36. M. Bosco, P. Bisseret, C. Bouix-Peter, and J. Eustache, "A New Concise Synthesis of Nectrisine and Its Facile Conversion to Phosphonoazasugars," *Tetrahedron Letters* 42 (2001): 7949–7952.

37. C. Chevrier, D. Le Nouen, A. Defoin, and C. Tarnus, "Synthesis of Amino-L-Lyxose Phosphonates as Fucosyl-Phosphate Mimics," *European Journal of Organic Chemistry* (2006): 2384–2392.

38. C. Cocaud, C. Nicolas, T. Poisson, X. Pannecoucke, C. Y. Legault, and O. R. Martin, "Tunable Approach for the Stereoselective Synthesis of 1-C-Diethylphosphono(difluoromethyl) Iminosugars as Glycosyl Phosphate Mimics," *The Journal of Organic Chemistry* 82 (2017): 2753–2763.

39. P. Merino, S. Franco, F. L. Merchan, and T. Tejero, "Nucleophilic Additions to Chiral Nitrones: New Approaches to Nitrogenated Compounds," *Synlett* 2000 (2000): 442–454.

40. A. Goti, S. Cicchi, V. Mannucci, et al., "Iterative Organometallic Addition to Chiral Hydroxylated Cyclic Nitrones: Highly Stereoselective Syntheses of Alpha, alpha'- and Alpha, alpha-Substituted Hydroxypyrrolidines," *Organic Letters* 5 (2003): 4235–4238.

41. I. Delso, E. Marca, V. Mannucci, T. Tejero, A. Goti, and P. Merino, "Tunable Diastereoselection of Biased Rigid Systems by Lewis Acid Induced Conformational Effects: A Rationalization of the Vinylation of Cyclic Nitrones En Route to Polyhydroxylated Pyrrolidines," *Chemistry–A European Journal* 16 (2010): 9910–9919.

42. O. Meyer, C. Grosdemange-Billiard, D. Tritsch, and M. Rohmer, "Isoprenoid Biosynthesis via the MEP Pathway. Synthesis of (3R,4S)-3,4-Dihydroxy-5-Oxohexylphosphonic Acid, an Isosteric Analogue of 1-Deoxy-d-Xylulose 5-Phosphate, the Substrate of the 1-Deoxy-d-Xylulose 5-Phosphate Reducto-Isomerase," *Organic & Biomolecular Chemistry* 1 (2003): 4367–4372.

43. X. Li, L. Yuan, Q. Wang, et al., "Solid-Phase Synthesis of a Special Phosphorylated Peptide as a Biomarker for LC–MS/MS Detection for OPNA Exposure," *Synlett* 28 (2017): 986–988.

44. A. Dondoni, F. Junquera, F. L. Merchan, P. Merino, M.-C. Scherrmann, and T. Tejero, "Stereoselective Addition of 2-Furyllithium and 2-Thiazolyllithium to Sugar Nitrones. Synthesis of Carbon-Linked Glycoglycines," *The Journal of Organic Chemistry* 62 (1997): 5484–5496.

45. P. Merino, S. Franco, F. L. Merchan, and T. Tejero, "Asymmetric Addition Reactions of Lithium (Trimethylsilyl)acetylide with Chiral a-Amino Nitrones. Synthesis of Diastereomerically Pure N-Hydroxy-a-Amino Acids," *The Journal of Organic Chemistry* 63 (1998): 5627–5630.

46. P. Merino, S. Franco, F. L. Merchan, J. Revuelta, and T. Tejero, "Efficient Synthesis of (2R,3S)- and (2S,3S)-2-Amino-1,3,4-Butanetriols through Stereodivergent Hydroxymethylation of D-Glyceraldehyde Nitrones," *Tetrahedron Letters* 43 (2002): 459–462.

47. A. J. Cohen, P. Mori-Sánchez, and W. Yang, "Challenges for Density Functional Theory," *Chemical Reviews* 112 (2012): 289–320.

48. D. B. Berkowitz and D. G. Sloss, "Diallyl (Lithiodifluoromethyl)phosphonate: A New Reagent for the Introduction of the (Difluoromethylene) phosphonate Functionality," *The Journal of Organic Chemistry* 60 (1995): 7047–7050.

49. D. R. Vutukuri, P. Bharathi, Z. Yu, K. Rajasekaran, M.-H. Tran, and S. Thayumanavan, "A Mild Deprotection Strategy for Allyl-Protecting Groups and Its Implications in Sequence Specific Dendrimer Synthesis," *The Journal of Organic Chemistry* 68 (2003): 1146–1149.

50. T. Li, A. Tikad, W. Pan, and S. P. Vincent, "β-Stereoselective Phosphorylations Applied to the Synthesis of ADP- and Polyprenyl-β-Mannopyranosides," *Organic Letters* 16 (2014): 5628–5631.

51. M. Strenkowska, P. Wanat, M. Ziemniak, J. Jemielity, and J. Kowalska, "Preparation of Synthetically Challenging Nucleotides Using Cyanoethyl P-Imidazolides and Microwaves," *Organic Letters* 14 (2012): 4782–4785.

52. J. Stepinski, M. Bretner, M. Jankowska, et al., "Synthesis and Properties of P1, P2-, P1, P3- and P1, P4-Dinucleoside Di-, Tri- and Tetraphosphate mRNA. 5′-CAP Analogs," *Nucleosides, Nucleotides & Nucleic Acids* 14 (1995): 717–721.

53. J. Angulo and P. M. Nieto, "STD-NMR: Application to Transient Interactions between Biomolecules-a Quantitative Approach," *European Biophysics Journal* 40 (2011): 1357–1369.

54. N. R. Krishna and V. Jayalakshmi, "Quantitative Analysis of STD-NMR Spectra of Reversibly Forming Ligand-Receptor Complexes," *Topics in Current Chemistry* 273 (2008): 15–54.

55. A. Gimeno, L. M. Santos, M. Alemi, et al., "Insights on the Interaction between Transthyretin and Aβ in Solution. A Saturation Transfer Difference (STD) NMR Analysis of the Role of Iododiflunisal," *Journal of Medicinal Chemistry* 60 (2017): 5749–5758.

56. R. P. Venkitakrishnan, O. Benard, M. Max, J. L. Markley, and F. M. Assadi-Porter, "Use of NMR Saturation Transfer Difference Spectroscopy to Study Ligand Binding to Membrane Proteins," *Membrane Protein Structure and Dynamics: Methods and Protocols* 914 (2012): 47–63.

57. C. Airoldi, S. Giovannardi, B. La Ferla, J. Jiménez-Barbero, and F. Nicotra, "Saturation Transfer Difference NMR Experiments of Membrane Proteins in Living Cells under HR-MAS Conditions: The Interaction of the SGLT1 Co-Transporter with Its Ligands," *Chemistry–A European Journal* 17 (2011): 13395–13399.

58. S. Mari, D. Serrano-Gómez, F. J. Cañada, A. L. Corbí, and J. Jiménez-Barbero, "1D Saturation Transfer Difference NMR Experiments on Living Cells: The DC-SIGN/Oligomannose Interaction," *Angewandte Chemie International Edition* 44 (2005): 296–298.

59. T. Haselhorst, A. C. Lamerz, and M. Itzstein, "Saturation Transfer Difference NMR Spectroscopy as a Technique to Investigate Protein-Carbohydrate Interactions in Solution," *Methods in Molecular Biology* 534 (2009): 375–386.

60. S. Robakiewicz, C. Bridot, S. Serna, et al., "Minimal Epitope for Mannitou IgM on Paucimannose-Carrying Glycoproteins," *Glycobiology* 31 (2021): 1005–1017.

61. A. Garcia-Garcia, S. Serna, Z. Yang, et al., "FUT8-Directed Core Fucosylation of N-Glycans Is Regulated by the Glycan Structure and Protein Environment," *ACS Catalysis* 11 (2021): 9052–9065.

62. S. Monaco, J. Angulo, and M. Wallace, "Imaging Saturation Transfer Difference (STD) NMR: Affinity and Specificity of Protein–Ligand Interactions From a Single NMR Sample," *Journal of the American Chemical Society* 145 (2023): 16391–16397.

63. S. Monaco, J. Browne, M. Wallace, J. Angulo, and L. Stokes, "On-Cell Saturation Transfer Difference NMR Spectroscopy on Ion Channels: Characterizing Negative Allosteric Modulator Binding Interactions of P2X7," *Journal of the American Chemical Society* 147 (2025): 32400–32411.

64. H. Wang, K. Tachibana, Y. Zhang, et al., "Cloning and Characterization of a Novel UDP-GalNAc: Polypeptide N-Acetylgalactosaminyltransferase, Pp-GalNAc-T14," *Biochemical and Biophysical Research Communications* 300 (2003): 738–744.

65. C. Peng, A. Togayachi, Y. D. Kwon, et al., "Identification of a Novel Human UDP-GalNAc Transferase with Unique Catalytic Activity and Expression Profile," *Biochemical and Biophysical Research Communications* 402 (2010): 680–686.

66. E. P. Bennett, U. Mandel, H. Clausen, T. A. Gerken, T. A. Fritz, and L. A. Tabak, "Control of Mucin-Type O-Glycosylation: A Classification of the Polypeptide GalNAc-Transferase Gene Family," *Glycobiology* 22 (2012): 736–756.

67. L. R. M. de, E. Lira-Navarrete, T. A. Gerken, and R. Hurtado-Guerrero, "Polypeptide GalNAc-Ts: From Redundancy to Specificity," *Current Opinion in Structural Biology* 56 (2019): 87–96.

68. E. Lira-Navarrete, M. de las Rivas, I. Companon, et al., "Dynamic Interplay between Catalytic and Lectin Domains of GalNAc-Transferases Modulates Protein O-Glycosylation," *Nature Communications* 6 (2015): 6937.

69. A. M. L. A. I. S. T. ByteDance, X. Chen, Y. Zhang, et al., *Protenix - Advancing Structure Prediction Through a Comprehensive AlphaFold3 Reproduction*," 2025, preprint bioRxiv, 2025.2001.2008.631967.

70. R. A. Friesner, J. L. Banks, R. B. Murphy, et al., "Glide: A New Approach for Rapid, Accurate Docking and Scoring. 1. Method and Assessment of Docking Accuracy," *Journal of Medicinal Chemistry* 47 (2004): 1739–1749.

71. T. A. Halgren, R. B. Murphy, R. A. Friesner, et al., "Glide: A New Approach for Rapid, Accurate Docking and Scoring. 2. Enrichment Factors in Database Screening," *Journal of Medicinal Chemistry* 47 (2004): 1750–1759.

72. E. Lira-Navarrete, J. Iglesias-Fernández, W. F. Zandberg, et al., "Substrate-Guided Front-Face Reaction Revealed by Combined Structural Snapshots and Metadynamics for the Polypeptide N-Acetylgalactosaminyltransferase 2," *Angewandte Chemie International Edition* 53 (2014): 8206–8210.

73. P. Merino, R. H. Guerrero, I. Delso, and T. Tejero, (Unpublished results).

74. M. J. Frisch, G. W. Trucks, H. B. Schlegel, et al., Frisch, Gaussian 16. Revision C01, 2016.

75. J.-D. Chai and M. Head-Gordon, "Long-Range Corrected Hybrid Density Functionals with Damped Atom–atom Dispersion Corrections," *Physical Chemistry Chemical Physics : PCCP* 10 (2008): 6615–6620.

76. F. Weigend, "Accurate Coulomb-Fitting Basis Sets for H to Rn," *Physical Chemistry Chemical Physics : PCCP* 8 (2006): 227–236.

77. F. Weigend and R. Ahlrichs, "Balanced Basis Sets of Split Valence, Triple Zeta Valence and Quadruple Zeta Valence Quality for H to Rn: Design and Assessment of Accuracy," *Physical Chemistry Chemical Physics : Pccp* 7 (2005): 3297–3305.

78. A. V. Marenich, C. J. Cramer, and D. G. Truhlar, "Universal Solvation Model Based on Solute Electron Density and on a Continuum Model of the Solvent Defined by the Bulk Dielectric Constant and Atomic Surface Tensions," *The Journal of Physical Chemistry. B* 113 (2009): 6378–6396.

79. R. Tanaka, M. Yamashita, L. W. Chung, K. Morokuma, and K. Nozaki, "Mechanistic Studies on the Reversible Hydrogenation of Carbon Dioxide Catalyzed by an Ir-PNP Complex," *Organometallics* 30 (2011): 6742–6750.

80. C. Y. Legault, "*CYLview, 1.0b, Université de Sherbrooke*," 2009, accessed December 1, 2025, http://www.cylview.org.

81. J. Jumper, R. Evans, A. Pritzel, et al., "Highly Accurate Protein Structure Prediction with AlphaFold," *Nature* 596 (2021): 583–589.

82. W. L. Jorgensen, D. S. Maxwell, and J. Tirado-Rives, "Development and Testing of the OPLS All-Atom Force Field on Conformational Energetics and Properties of Organic Liquids," *Journal of the American Chemical Society* 118 (1996): 11225–11236.

83. D. A. Case, et al., University of California, San Francisco AMBER. 2020 (for the Full Reference See SI).

84. J. Wang, W. Wang, P. A. Kollman, and D. A. Case, "Automatic Atom Type and Bond Type Perception in Molecular Mechanical Calculations," *Journal of Molecular Graphics and Modelling* 25 (2006): 247–260.

85. J. A. Maier, C. Martinez, K. Kasavajhala, L. Wickstrom, K. E. Hauser, and C. Simmerling, "ff14SB: Improving the Accuracy of Protein Side Chain and Backbone Parameters From ff99SB," *Journal of Chemical Theory and Computation* 11 (2015): 3696–3713.

86. W. L. Jorgensen, J. Chandrasekhar, J. D. Madura, R. W. Impey, and M. L. Klein, "Comparison of Simple Potential Functions for Simulating Liquid Water," *The Journal of Chemical Physics* 79 (1983): 926.

87. R. L. Davidchack, R. Handel, and M. V. Tretyakov, "Langevin Thermostat for Rigid Body Dynamics," *The Journal of Chemical Physics* 130 (2009): 234101.

88. T. Darden, D. York, and L. Pedersen, "Particle Mesh Ewald: An N·log(N) Method for Ewald Sums in Large Systems," *The Journal of Chemical Physics* 98 (1993): 10089–10092.

Supporting Information

Additional supporting Information can be found online in the Supporting Information section. The authors have cited additional references within the SI [86–88]. **Supporting Fig. S1:** STD NMR (trace blue) of compound **3d**. Shadowed squares indicates the epitope corresponding to the atoms of the same color. **Supporting Fig. S2:** STD-NMR (trace blue) of compound **3e**. Shadowed squares indicate the epitope corresponding to the atoms of the same color. **Supporting Fig. S3:** Nitrones N1-3. **Supporting Fig. S4**: Affinity studies for UDP and compound **3e** with GalNAc-T2. **Supporting Fig. S4:** Encounter pairs **EPa–c**. **Supporting Fig. S5:** (a) Map of interactions of 3e with GalNAc-T2 in the catalytic domain according to docking made with Glide [11–12] in Maestro as implemented in Schrodinger. [13] (b) Interactions of 3e in the catalytic site of GalNAc-T2. **Supporting Fig. S6:** Overlapping of the structures of GalNAc's T2 (from X-ray crystallography; PDB ID: 4D0Z), T14 an T16 (both predicted with Protenix). The catalytic domains of the three enzymes are superimposable, whereas the lectin domain of T16 has a different orientation of T2 and T14. The peptide linker is colored red in all cases. The lectin domain is given in dark green for GalNAc-T2, marine for GalNAc-T12, and magenta for GalNAc-T16, and the catalytic domain is given in green for GalNAc-T2, cyan for GalNAc-T12, and tint for GalNAc-T16. **Supporting Fig. S7:** Predicted (Protenix) [14] structures for complexes between 3e and GalNAc-T2 (a), GalNAc-T14 (b), and GalNAc-T16 (c). These structures have been employed as starting points for the MD simulations. The peptide linker is colored red in all cases. The lectin domain is given in dark green for GalNAc-T2, marine for GalNAc-T12, and magenta for GalNAc-T16, and the catalytic domain is given in green for GalNAc-T2, cyan for GalNAc-T12, and tint for GalNAc-T16. **Supporting Fig. S8:** RMSD for GalNAc-T2 (left), T14 (middle), and T16 (right). **Supporting Table S1:** Calculated (b3lyp-gd3bj/def2tzvp/smd=THF//b3lyp-gd3bj/def2svp/smd=THF) absolute (hartree) and relative (kcal/mol) free energies for reagents, encounter pairs and transition structures corresponding to the addition of the lithium anion of **7a** to nitrone **N1**. **Supporting Table S2:** Calculated (b3lyp-gd3bj/def2tzvp/smd=THF//b3lyp-gd3bj/def2svp/smd=THF) absolute (hartree) and relative (kcal/mol) free energies for reagents, encounter pairs and transition structures corresponding to the addition of the lithium anion of **7a** to nitrone **N2**. **Supporting Table S3:** Calculated (b3lyp-gd3bj/def2tzvp/smd=THF//b3lyp-gd3bj/def2svp/smd=THF) absolute (hartree) and relative (kcal/mol) free energies for reagents, encounter pairs and transition structures corresponding to the addition of the lithium anion of **7a** to nitrone **N3**. **Supporting Table S4:** Calculated (wb97xd/def2tzvp/smd=THF//wb97xd/def2svp/smd=THF) absolute (hartree) and relative (kcal/mol) free energies for reagents, encounter pairs and transition structures corresponding to the addition of the lithium anion of **7a** to nitrone **N1**. **Supporting Table S5:** Calculated (wb97xd/def2tzvp/smd=THF//wb97xd/def2svp/smd=THF) absolute (hartree) and relative (kcal/mol) free energies for reagents, encounter pairs and transition structures corresponding to the addition of the lithium anion of **7a** to nitrone **N2**. **Supporting Table S6:** Calculated (wb97xd/def2tzvp/smd=THF//wb97xd/def2svp/smd=THF) absolute (hartree) and relative (kcal/mol) free energies for reagents, encounter pairs and transition structures corresponding to the addition of the lithium anion of **7a** to nitrone **N3**. **Supporting Table S7:** Conservation of hydrophobic pockets in GalNAc-T2, T14, and T16.